



This is a repository copy of *Multipoint detection of GRB221009A's propagation through the heliosphere.*

White Rose Research Online URL for this paper:

<https://eprints.whiterose.ac.uk/204084/>

Version: Published Version

---

**Article:**

Voshchepynets, A. [orcid.org/0000-0001-8307-781X](https://orcid.org/0000-0001-8307-781X), Agapitov, O.V. [orcid.org/0000-0001-6427-1596](https://orcid.org/0000-0001-6427-1596), Wilson, L. [orcid.org/0000-0002-4313-1970](https://orcid.org/0000-0002-4313-1970) et al. (9 more authors) (2023) Multipoint detection of GRB221009A's propagation through the heliosphere. *The Astrophysical Journal Letters*, 956 (1). ISSN 2041-8205

<https://doi.org/10.3847/2041-8213/acf933>

---

**Reuse**

This article is distributed under the terms of the Creative Commons Attribution (CC BY) licence. This licence allows you to distribute, remix, tweak, and build upon the work, even commercially, as long as you credit the authors for the original work. More information and the full terms of the licence here:

<https://creativecommons.org/licenses/>

**Takedown**

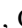











If you consider content in White Rose Research Online to be in breach of UK law, please notify us by emailing [eprints@whiterose.ac.uk](mailto:eprints@whiterose.ac.uk) including the URL of the record and the reason for the withdrawal request.



[eprints@whiterose.ac.uk](mailto:eprints@whiterose.ac.uk)  
<https://eprints.whiterose.ac.uk/>



# Multipoint Detection of GRB221009A’s Propagation through the Heliosphere

Andrii Voshchepynets<sup>1,2</sup> , Oleksiy V. Agapitov<sup>2,3</sup> , Lynn Wilson III<sup>4</sup> , Vassilis Angelopoulos<sup>5</sup> , Samer T. Alnussirat<sup>2</sup> , Michael Balikhin<sup>6</sup> , Myroslava Hlebena<sup>1</sup> , Ihor Korol<sup>7,8</sup> , Davin Larson<sup>2</sup> , David Mitchell<sup>2</sup> , Christopher Owen<sup>9</sup> , and Ali Rahmati<sup>2</sup> 

<sup>1</sup> Department of System Analysis and Optimization Theory, Uzhhorod National University, Uzhhorod, Ukraine

<sup>2</sup> Space Sciences Laboratory, University of California, Berkeley, CA 94720, USA

<sup>3</sup> Astronomy and Space Physics Department, National Taras Shevchenko University of Kyiv, Kyiv, Ukraine

<sup>4</sup> Goddard Space Flight Center, National Aeronautics and Space Administration, Greenbelt, MD, USA

<sup>5</sup> Department of Earth, Planetary, and Space Sciences, University of California, Los Angeles, CA, USA

<sup>6</sup> University of Sheffield, Sheffield, UK

<sup>7</sup> Department of Algebra and Differential Equation, Uzhhorod National University, Uzhhorod, Ukraine

<sup>8</sup> Department of Mathematical Analysis, The John Paul II Catholic University of Lublin, Lublin, Poland

<sup>9</sup> Mullard Space Science Laboratory, University College London, Dorking RH5 6NT, UK

Received 2023 July 25; revised 2023 August 28; accepted 2023 September 11; published 2023 October 5

## Abstract

We present the results of processing the effects of the powerful gamma-ray burst GRB221009A captured by the charged particle detectors (electrostatic analyzers and solid-state detectors) on board spacecraft at different points in the heliosphere on 2022 October 9. To follow the GRB221009A propagation through the heliosphere, we used the electron and proton flux measurements from solar missions Solar Orbiter and STEREO-A; Earth’s magnetosphere and solar wind missions THEMIS and Wind; meteorological satellites POES15, POES19, and MetOp3; and MAVEN—a NASA mission orbiting Mars. GRB221009A had a structure of four bursts: the less intense Pulse 1—the triggering impulse—was detected by gamma-ray observatories at  $T_0 = 13:16:59$  UT (near the Earth); the most intense Pulses 2 and 3 were detected on board all the spacecraft from the list; and Pulse 4 was detected in more than 500 s after Pulse 1. Due to their different scientific objectives, the spacecraft, whose data were used in this study, were separated by more than 1 au (Solar Orbiter and MAVEN). This enabled the tracking of GRB221009A as it was propagating across the heliosphere. STEREO-A was the first to register Pulse 2 and 3 of the GRB, almost 100 s before their detection by spacecraft in the vicinity of Earth. MAVEN detected GRB221009A Pulses 2, 3, and 4 at the orbit of Mars about 237 s after their detection near Earth. By processing the observed time delays, we show that the source location of the GRB221009A was at R.A.  $288^\circ.5$ , decl.  $18^\circ.5 \pm 2^\circ$  (J2000).

*Unified Astronomy Thesaurus concepts:* [Gamma-ray bursts \(629\)](#)

## 1. Introduction

GRB221009A was a bright and long-lasting gamma-ray burst (GRB) detected by the spaceborne telescopes such as the Burst Alarm Telescope (BAT) on board Swift (Dichiara et al. 2022; afterglow), Gamma-ray Burst Monitor (GBM) and Large Area Telescope (LAT) on board the Fermi Gamma-ray Space Telescope (FGST) (Veres et al. 2022; Lesage et al. 2022; Pillera et al. 2022), AGILE (Piano et al. 2022; Ursi et al. 2022), INTEGRAL SPI-ACS (Gotz et al. 2022), Solar Orbiter (Xiao et al. 2022), SRG/ART-XC (Lapshov et al. 2022), Konus-Wind (Frederiks et al. 2022), GRBAlpha (Ripa et al. 2022), and STPSat-6 (Mitchell et al. 2022), High Energy Burst Searcher (HEBS) on SATech-01 (Liu et al. 2022), BepiColombo (Kozyrev et al. 2022), and by the ground observatories such as the Large High Altitude Air Shower Observatory (LHAASO; Brdar & Li 2023). The GRB221009A started with a precursor at  $T_0 = 2022$  October 9 13:16:59 UTC (Pulse 1), followed by a set of pulses at  $\sim T_0 + 225$  s (Pulse 2),  $\sim T_0 + 256$  s (Pulse 3), and  $\sim T_0 + 509$ s (Pulse 4) (GRB Coordinates Network; GCN Veres et al. 2022; Liu et al. 2022; Rodi & Ubertini 2023). The afterglow of the burst outshone all

other GRBs seen before (Sahu et al. 2023) in a very-high-energy (VHE) band. The water Cherenkov detector array and the larger air shower kilometer square area detector at LHAASO observed more than 5000 VHE photons in the 500 GeV–18 TeV energy range within 2000 s from the trigger, making them the most energetic photons ever observed from a GRB (Baktash et al. 2022). The multiwavelength afterglow and comparative brightness of the GRB221009A were studied in Laskar et al. (2023) and Kann et al. (2023). The event was so long and intense that the increased ionization by X- and gamma-ray emission caused sudden global ionospheric disturbances in the D region of Earth’s ionosphere (Hayes & Gallagher 2022; Pal et al. 2023).

The source location of the GRB has been derived to be centered at R.A. =  $288^\circ.282$  and decl. =  $19^\circ.495$  (J2000) with a 90% containment radius of  $0^\circ.027$  (Pillera et al. 2022) and its redshift was estimated to be  $z = 0.15$  (Veres et al. 2022; de Ugarte Postigo et al. 2022). The relatively small value of the redshift indicates that this is one of the closest observed long-duration GRBs (Rastinejad et al. 2022; Troja et al. 2022; Mei et al. 2022; Gompertz et al. 2023) as its luminosity distance is  $\approx 720$  Mpc (O’Connor et al. 2023) based on the  $\Lambda$ CDM cosmological model (Freedman 2021). Even after taking into account the proximity, the GRB221009A remains one of the most luminous explosions to date (O’Connor et al. 2023), with lower limits of isotropic-equivalent gamma-ray energy

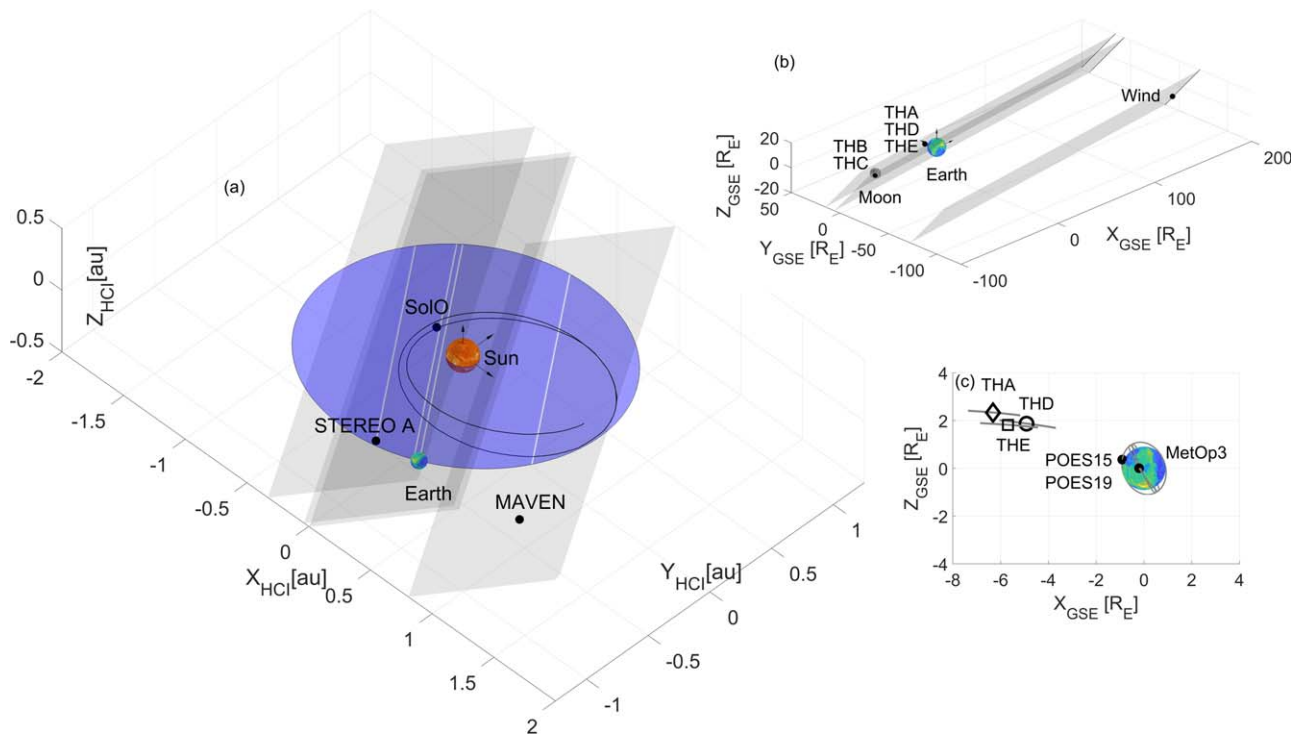


**Figure 1.** The configuration of the spacecraft during the GRB211211A event: (a) location of STEREO-A, SoLO, and MAVEN in the Heliocentric Inertial (HCI) coordinate system. The Earth’s orbit is shown in blue. (b) and (c) Locations of THEMIS and POES/MetOp spacecraft in the Geocentric Solar Ecliptic (GSE) coordinate system. The propagation of the GRB221009A across the heliosphere is schematically shown with the set of planes.

$\gtrsim 3 \times 10^{54}$  erg measured over the energy range from 20 keV to 10 MeV (Frederiks et al. 2022; de Ugarte Postigo et al. 2022; Kann & Agui Fernandez 2022) and the more precise value of  $\gtrsim 1.2 \times 10^{55}$  (Frederiks et al. 2023; Lesage et al. 2023).

In this article, we present the analysis of observations of GRB221009A by the charged particle detectors on board various spacecraft located at different points across the heliosphere on 2022 October 9. Data from charged particle detectors on board heliosphere spacecraft can provide an additional perspective on the GRB that complements observations from the gamma-ray telescopes (Schwartz et al. 2005; Terasawa et al. 2005). Charged particle detectors, despite not being designed to detect high-energy gamma-ray photons, can measure the flux of secondary particles produced within the material of the spacecraft (Pisacane 2005) or the detector itself (Battiston et al. 2023). GRB221009A has been previously studied using data from the electrostatic analyzer and solid-state telescopes on board the THEMIS mission (Agapitov et al. 2023), the HEPP-L charged particle detector on board the low Earth orbit (LEO) China Seismo-Electromagnetic Satellite (Battiston et al. 2023), and MEPED on board POES/MetOp (Vitale et al. 2023). It was shown that the high-time resolution of the electron and proton flux measurements (up to 8 measurements per second Agapitov et al. 2023) reveal the structure of the intense bursts (Pulses 2, 3, and 4) and were shown to follow quite well the fine inner structure of the Pulses 2 and 3 of the GRB221009A signal recorded by HEBS with 0.05 s resolution (Liu et al. 2022). Here we present observations of the GRB221009A by the charged particle detectors of STEREO-A, Solar Orbiter (SoLO), Wind, THEMIS, POES/MetOp, and MAVEN spacecraft. STEREO-A (Kaiser et al. 2008) and SoLO (Müller et al. 2020) are Sun observing missions. Wind (Wilson et al. 2021) and THEMIS

(Sibeck & Angelopoulos 2008) are the missions dedicated to studying processes in the solar wind and Earth’s magnetosphere. POES (Rodger et al. 2010) and MetOp (Selesnick et al. 2020) are a constellation of polar-orbiting weather satellites. MAVEN (Jakosky et al. 2015) is the NASA mission to study atmospheric losses at Mars. The spacecraft locations are shown in Figure 1. The description of the missions’ particle flux measurements is in Section 2. The multipoint observations of the GRB221009A effects and the results of timing processing are in Sections 3 and 4. The conclusion section contains a short description of the obtained results.

## 2. Data Description

### 2.1. SoLO Data

The SoLO mission is a joint ESA and NASA project, which aims to study how the Sun creates and controls the heliosphere (Müller et al. 2020; Owen et al. 2020). SoLO has a comprehensive set of remote-sensing and in situ probing instruments that enable correlative studies of the solar wind plasma—its origin, transport processes, and elemental composition. The Energetic Particle Detector (EPD) (Rodríguez-Pacheco et al. 2020) on board SoLO is composed of four units: the Supra-Thermal Electrons and Protons, the Electron Proton Telescope (EPT), the Suprathermal Ion Spectrograph, and the High-Energy Telescope (HET). For this study, we used data provided by the EPT. The EPT consists of two double-ended telescopes: EPT 1 is pointing sunward and antisunward along the nominal Parker spiral while EPT-HET 2 is pointing northward and southward. The EPT relies on the magnet/foil technique to separate and measure electrons and protons in the energy range [0.03–0.43] MeV for electrons and

[0.05–5.83] MeV for protons. EPT sensors are able to collect data with a cadence of up to 1 s.

## 2.2. STEREO-A Data

The twin STEREO spacecraft, A and B, were launched on 2006 October 26. The purpose of the mission is to understand the causes and mechanisms of coronal mass ejection (Kaiser et al. 2008). As of now, only STEREO-A is still operational. In this study, we used data gathered by the In situ Measurements of Particles And CME Transients (IMPACT) suite of instruments, which measures the flux of solar wind electrons, energetic electrons, protons, and heavier ions (Luhmann et al. 2008). The Suprathermal Electron (STE) instrument, part of the IMPACT, is designed to measure the  $\sim 2$ –100 keV suprathermal electrons in the interplanetary medium near 1 au. STE utilizes silicon semiconductor detectors that measure all energies simultaneously, and has a temporal resolution of 10 s.

## 2.3. Wind Data

The Wind spacecraft is a part of the Global Geospace Science program (GGS), a subset of the International Solar-Terrestrial Physics program, designed to study basic plasma processes occurring in the near-Earth solar wind (Acuña et al. 1995). Wind currently orbits at the first Lagrange point, about  $\sim 200 R_E$  sunward from Earth. It carries a comprehensive set of instruments, including a gamma-ray spectrometer KONUS (Aptekar et al. 1995) and a particle experiment, Three-Dimensional Plasma and Energetic Particle Investigation (3DP; Lin et al. 1995). KONUS is a gamma-ray spectrometer designed primarily for the detection and study of cosmic GRBs, with capabilities for the study of solar flares in the hard X-ray region (Wilson et al. 2021; Lysenko et al. 2022). The 3DP consists of three detector systems: the semiconductor detector telescopes (SST), the electron electrostatic analyzers (EESA), and the ion electrostatic analyzers (PESA). The SST consists of three arrays, each with a pair of double-ended telescopes to measure electron and ion fluxes above 20 keV. EESA and PESA are electrostatic analyzers that measure particle fluxes in a wide range of energies from 3 eV to 30 keV.

## 2.4. THEMIS Data

Time History of Events and Macroscale Interactions during Substorms (THEMIS) was designed to carry out multipoint investigations of substorm phenomena in the tail of the terrestrial magnetosphere (Sibeck & Angelopoulos 2008). It consists of five identically equipped satellites, which carry ElectroStatic Analyzers (ESA) and Solid-State Telescopes (SST) particle detectors (McFadden et al. 2008). THEMIS ESA is a pair of back-to-back top hat hemispherical electrostatic analyzers that measure the distribution functions of ions (0.005–25 keV) and electrons (0.005–30 keV) over  $4\pi$  str at  $22.5 \times 22.5$  angular resolution,  $\Delta E/E$  30% energy resolution, and 3s temporal resolution (4 s for the two ARTEMIS spacecraft orbiting the Moon; Angelopoulos 2014; the Acceleration, Reconnection, Turbulence, and Electrodynamics of the Moons Interaction with the Sun mission) time resolution plasma moments (McFadden et al. 2008). SST measures the superthermal (0.03–1 MeV) part of the ion and electron distributions over  $4\pi$  str with similar energy, angular, and temporal resolution. Combining the energy and solid-angle

measurements can sufficiently improve time resolution (up to a subsecond cadence; Agapitov et al. 2023).

## 2.5. POES and MetOp Data

Polar Orbiting Environmental Satellites (POES) and Meteorological Operational Satellites (MetOp) are a series of polar-orbiting meteorological satellites operated by NOAA and EUMETSAT on LEO orbits (Rodger et al. 2010; Selesnick et al. 2020). The current spacecraft generation—POES 15, 19, and three MetOp satellites are equipped with the same instruments, Medium Energy Proton and Electron Detector (MEPED), which is a subsystem of Space Environment Monitor (Pettit et al. 2021). MEPED is a set of solid-state energetic particle detectors that monitor the intensities of proton and electron flux over an energy range extending from 30 keV to  $\sim 7$  MeV, for protons, and up to 2.5 MeV, for electrons, with a 2 s cadence.

## 2.6. MAVEN Data

The Mars Atmosphere and Volatile EvolutionN (MAVEN) is a NASA mission dedicated to studying the ionosphere and upper atmosphere of Mars, its interactions with the Sun, and the solar wind (Jakosky et al. 2015). The spacecraft carries a comprehensive set of charged particle measurement instruments designed to study losses of the ionospheric plasma due to interaction with the solar wind. It consists of the SolarWind Electron Analyzer (SWEA), the Solar Wind Ion Analyzer (SWIA), the Solar Energetic Particle (SEP) instrument, and the Supra-Thermal And Thermal Ion Composition (STATIC) instrument. SWEA is a top hat electrostatic analyzer utilizing electrostatic deflectors to provide a field of view of  $360^\circ \times 120^\circ$  and measures electrons between energies of 3 eV and 5 keV with a 2 s cadence (Mitchell et al. 2016). The SWIA is an electrostatic analyzer that measures the energy and angular distributions of solar wind and magnetosheath ions with a 4 s cadence (Halekas et al. 2015). It uses deflection optics, which provide a broad  $360^\circ \times 90^\circ$  field of view and has a broad energy range of 5 eV to 25 keV. SEP consists of two sensors, each utilizing a dual, double-ended solid-state detector telescope that measures fluxes of electrons from 20 to 1000 keV and ions from 20 to 6000 keV (Larson et al. 2015). SEP measurements have a 2 s time cadence. STATIC is an electrostatic top hat analyzer designed to measure the cold ion of the Martian ionosphere, the heated suprathermal tail of the plasma in the upper ionosphere, and the pickup ions (McFadden et al. 2015). It operates over an energy range of 0.1 eV up to 30 keV, with a base time resolution of 4 s. STATIC utilizes electrostatic deflectors that provide a field of view of  $360^\circ \times 90^\circ$ .

Table 1 summarizes the parameters of the instruments used in this publication.

## 3. Observations

Figure 1 shows the locations of the spacecraft during the GRB221009A. Panel (a) provides a general view of the spacecraft’s location in the Heliocentric coordinate (HCI) system (Fränz & Harper 2002). Relative to the Sun, SolO was the closest, at the heliocentric distance of  $\sim 0.30$  au (1 au  $\sim 499$  lt-s), followed by STEREO-A ( $\sim 0.96$  au), Earth, and MAVEN ( $\sim 1.46$  au). During the event, SolO was below the ecliptic plane (shown as a blue surface). Panels (b) and (c) show a

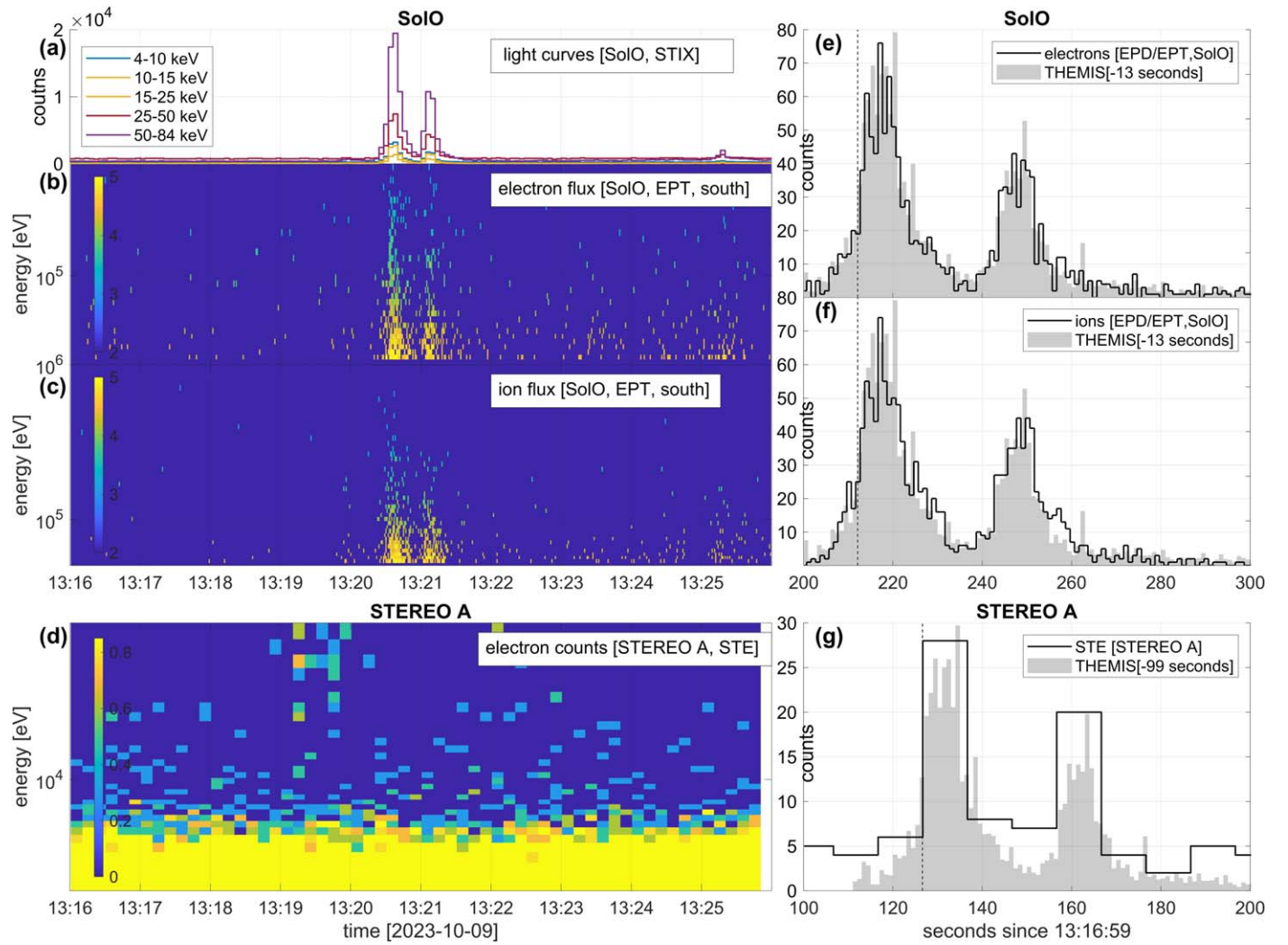


**Figure 2.** Detection of the effects of the GRB221009A by SoLo and STEREO-A: (a) light curves detected by STIX (SoLo); (b) and (c) electron and ion flux from EPT (SoLo); (d) electron counts from STE (STEREO-A); (e) and (f) integrated electron and ion counts from EPT (SoLo); (g) integrated electron counts from STE (STEREO-A). The background light-gray silhouette is the light curves of the combined THC and THC SST proton flux counts from (Agapitov et al. 2023).

**Table 1**  
Summary of the Instruments Used in This Study (the Energies Are in keV)

sc	SoLo	STEREO-A	THEMIS		Wind	POES/MetOp		MAVEN		
det	EPT	STE	ESA	SST	PESA	SST	MEPED	SWEA/SWIA	SEP	STATIC
$e^-$	30–420	20–100	5e-3–30	30–1e3		25–400	30–2.5e3	3e-3–30	20–1e3	
$i^+$	50–8.8e3		5e-3–25	0.03–1e3	3e-3–30	0.02–6e3	0.03–7e3	5e-3–25	0.02–6e3	1e-3–30

zoomed view of the configuration of the spacecraft in the vicinity of the Earth in the Geocentric Solar Ecliptic (GSE) coordinate system (Fränz & Harper 2002). The THEMIS mission (Sibeck & Angelopoulos 2008) consists of five identically equipped satellites (probes THA, THB, THC, THD, and THE). In 2011, two of the probes (THB and THC) were repurposed for the ARTEMIS mission and moved first to a Lissajous orbit around a lunar Lagrange point and a year later into highly eccentric, near-equatorial lunar orbit (Angelopoulos 2014). During the event, THB and THC were located near the Moon in the tail of Earth’s magnetosphere at geocentric distances of 58 and 61  $R_E$  (1  $R_E$  [Earth radius]

$\sim 0.021$  lt-s), while the inner THEMIS probes were at the geocentric distances of  $\sim 9$ – $10 R_E$ . Wind was further from the Earth to the sunward direction ( $x$ -axis) at the geocentric distance of  $\sim 203.26 R_E$  from the Earth. POES/MetOp spacecraft are on polar LEO orbits (panel (c) in Figure 1). The propagation of the GRB221009A in the heliosphere is schematically illustrated by the set of planar surfaces in Figure 1.

Xiao et al. (2022) reported the detection of GRB221009A by the Spectrometer/Telescope for Imaging X-rays (STIX; Krucker et al. 2020) on board SoLo (panel (a) in Figure 2). In addition, Pulses 2, 3, and 4 were captured by the EPT electron and proton detectors (they are shown in Figures 2(b)

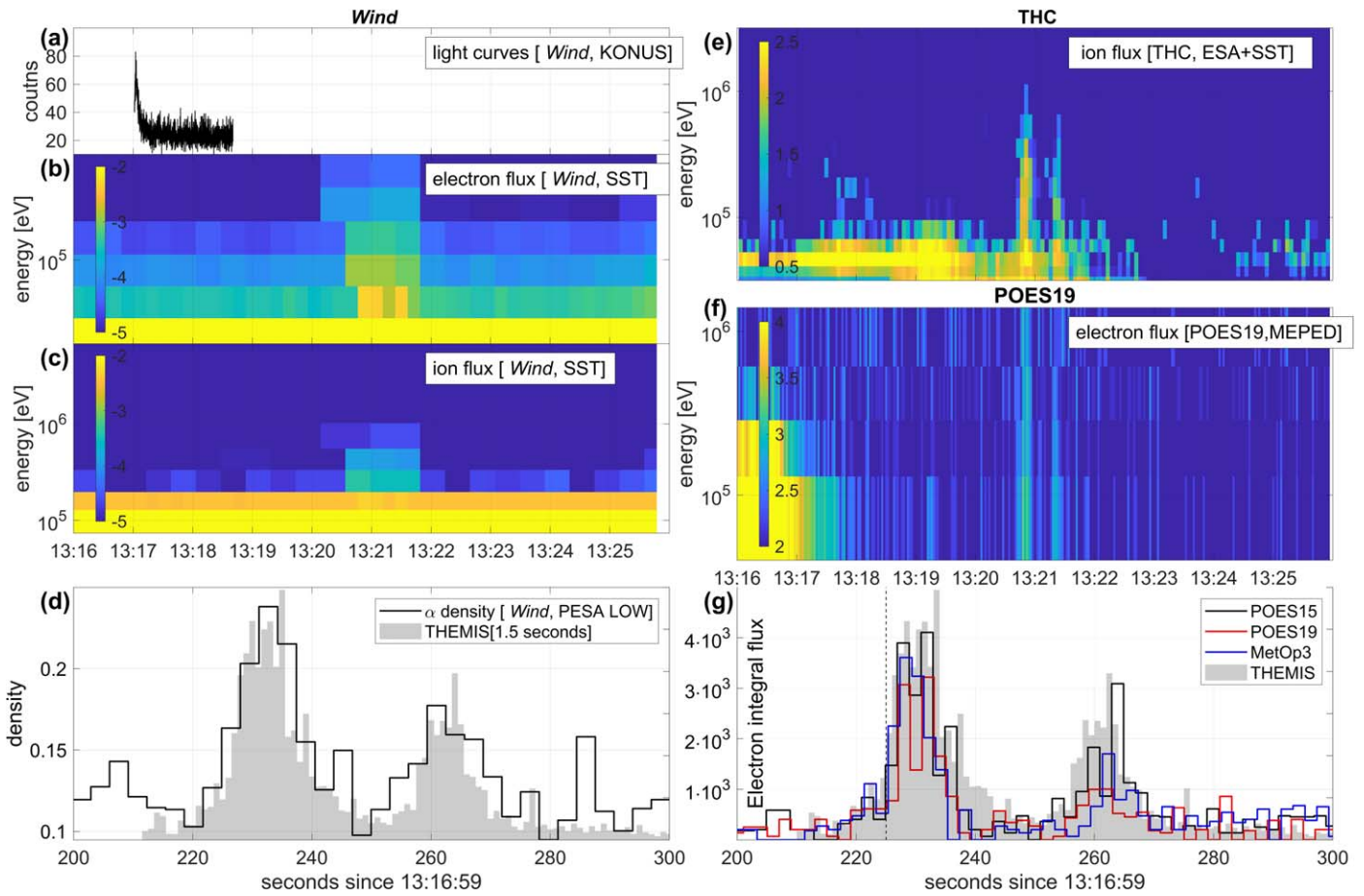


**Figure 3.** Detection of the effects of the GRB221009A by the spacecraft of Earth group: (a) light curve by KONUS (Wind; data available at [https://gcn.gsfc.nasa.gov/konus\\_grbs.html](https://gcn.gsfc.nasa.gov/konus_grbs.html)); (b) and (c) electron and ion flux by SST (Wind); (d) density of  $\alpha$ -particles by PESA (Wind); (e) ions flux by ESA+SST (THC); (f) electron flux by MEPED (POES19); and (g) the integrated electron flux by MEPED (POES15, POES19, and MetOp).

and (c), respectively). The electron and proton apparent flux enhancements associated with GRB221009A are observed at energies up to 0.5 MeV. Figures 2(e) and (f) show the integrated electron and proton counts in EPT 2 and the antisunward detector on EPT 1. For comparison, the shifted by  $-13$  s temporal profile measured by SST on THEMIS is shown in gray. The temporal profiles recorded by EPD follow quite well the profiles recorded on THEMIS (Agapitov et al. 2023) and HEPP-L (Battiston et al. 2023) but EPD detected GRB221009A  $\sim 13$  s earlier: the start of the main peak of Pulse 2 at  $\sim T_0 + 212$  s, and the start of Pulse 3 at  $\sim T_0 + 243$  s, compared to  $T_0 + 225$  s and  $T_0 + 256$  s reported in Agapitov et al. (2023;  $T_0 = 13:16:59.000$ , Veres et al. 2022). Data from STE on board STEREO-A are shown in Figure 2(d). GRB221009A-related signals were detected in the energy range from 20 to 100 keV at 13:19:06 (Pulse 2) and 13:19:36 (Pulse 3) almost 100 s earlier than they were detected by THEMIS (Agapitov et al. 2023). The STE time resolution of 10 s, is not sufficient to resolve details like shoulders (Liu et al. 2022) on the temporal profile of the burst (Figure 2(g)).

KONUS on board Wind detected the first Pulse of the GRB221009A at 13:17:01.648 (Frederiks et al. 2022; also shown in Figure 3(a)). Figures 3(b) and (c) show electron and ion flux measured by the Wind SST with 12 s resolution. The GRB221009A-related signals (Pulses 2 and 3) are visible in the lower-energy channels: 25–40 keV for electrons and 70–130 keV for ions. The related signal was also found in the  $\alpha$ -particle

density calculated on board from the PESA measurements. Comparing the temporal profile with the THEMIS measurements (Figure 3(d)) shows a time delay of  $\sim 1.5$  s.

The GRB221009A was detected by THEMIS ESA and SST on board the four THEMIS probes (THA, THB, THC, and THE). The signal appears as two very intense bursts at 13:20:36–13:21:30 and a subsequent less intense burst at around 13:25:30 (Figure 3(e)). The event was studied in detail by Agapitov et al. (2023). It was shown that the temporal profile of the burst with 0.25 s resolution can be obtained by combining the spin-resolved data from THB and THC Agapitov et al. (2023). Here we use the light curve of the combined THB and THC SST counts with 1 s resolution for comparison with the profiles detected by the other spacecraft used in this study.

Figure 3(f) shows electron flux measured by the POES 19 MEPED detector. The effects of the GRB221009A are visible as two relatively intense bursts detected within an energy range of 40 keV–1 MeV at 13:20:30–13:21:30. The temporal profiles of the GRB221009A-related signals recorded on POES 15, 19, and MetOp are shown in panel (g). The profile of Pulse 2 is very similar to that detected by THC, while the profile of Pulse 3 is much less prominent. The event was studied in detail by Vitale et al. (2023).

Figure 4 shows the observations of the GRB221009A made by the particle instruments on board MAVEN. The two very intense bursts—Pulses 2 and 3—were detected by all of the MAVEN particle instruments between 13:24:30 and 13:25:30,

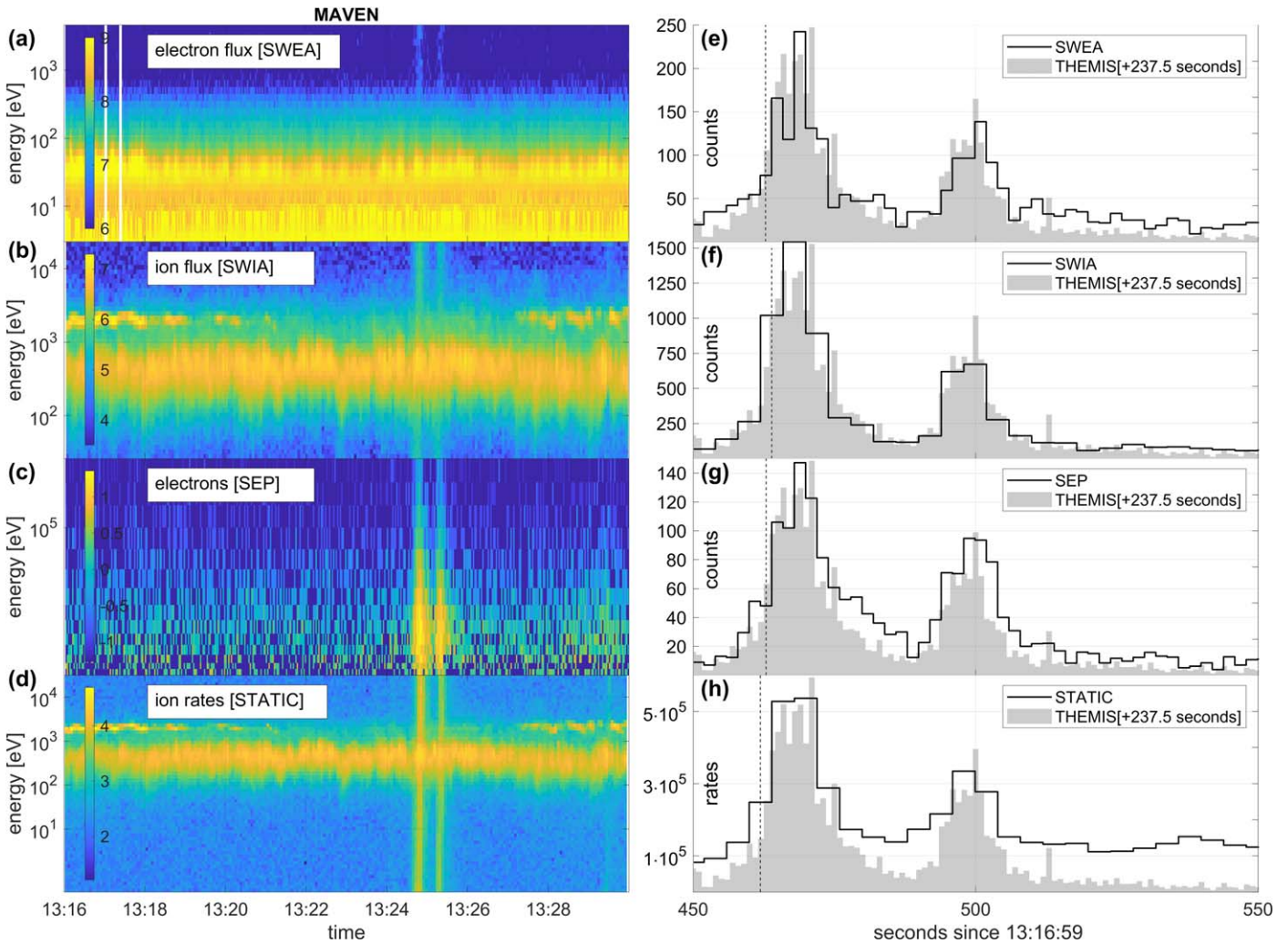


**Figure 4.** Detection of the effects of the GRB221009A by MAVEN: (a) electron flux by SWEA; (b) ion flux by SWIA; (c) electron counts by SEP; (d) ion rates by STATIC; (e)–(h) the integrated counts/rates from (a)–(d).

almost 4 minutes later than they were detected in the vicinity of the Earth (Earth–Mars distance at that time was  $\sim 0.73$  au or  $\sim 364$  lt-s). STATIC (Figure 4(d)) detected the third burst—Pulse 4—at 13:29:30. Measurements by the electrostatic analyzers are consistent, and the GRB221009A-related signal is visible in the ion data (SWIA and STATIC) through the entire energy range (up to 30 keV). In the electron measurements by SWEA, the signal was detected at the energies above  $\sim 1$  keV. Electron measurements by SEP show the effects of the GRB within the energy range from 20 to 200 keV. Comparison of the temporal profiles measured by MAVEN with the THEMIS observation (Figures 4(e)–(h)) shows a time delay of about 237.5 s.

High-energy gamma-ray photons mainly interact with the spacecraft and detector material via the electron–positron pair production process. The flux and energies of these secondaries are determined by the initial photons energy and flux as well as the thickness and density of the passive material of the spacecraft and detector itself. For this GRB, the spacecraft particle detectors mainly encountered energy deposition from the secondary charged particles (electrons and positrons). The simulation performed for the parameters of the HEPP-L telescope (Battiston et al. 2023) showed that 83% of the detected secondaries originate in the passive material around

the silicon detector and about 17% were directly generated within the detector. The secondary electrons also produce the signal recorded by the proton telescopes (and electrostatic analyzers; Agapitov et al. 2023), as was shown by the comparison of the electron fluxes measured by the electron and proton MEPED telescopes on board POES/MetOp (Vitale et al. 2023). The dilated study of the signal detected by SoLo and MAVEN will be a subject of the upcoming publications.

#### 4. Tracking Propagation of the GRB221009A across the Heliosphere

The multipoint observations of the GRB221009A signal propagation by the spacecraft at different locations enable estimation of the normal to the signal front (Paschmann & Daly 1998) and thus can be used to determine the direction to its source in the sky. Using THC spacecraft as a reference and assuming that the burst propagated as a planar front, one can find a normal  $\mathbf{n}$  to the front by solving a system of linear equations:

$$\sum_{\beta=1}^3 (r_{\beta}^{\alpha} - r_{\beta}^{\text{THC}}) n_{\beta} = v(T^{\alpha} - T^{\text{THC}}),$$

where  $\mathbf{r}$  is a position vector of the spacecraft,  $T$  is a time of observation,  $v$  is the speed of the front, and  $\alpha$  is the spacecraft:

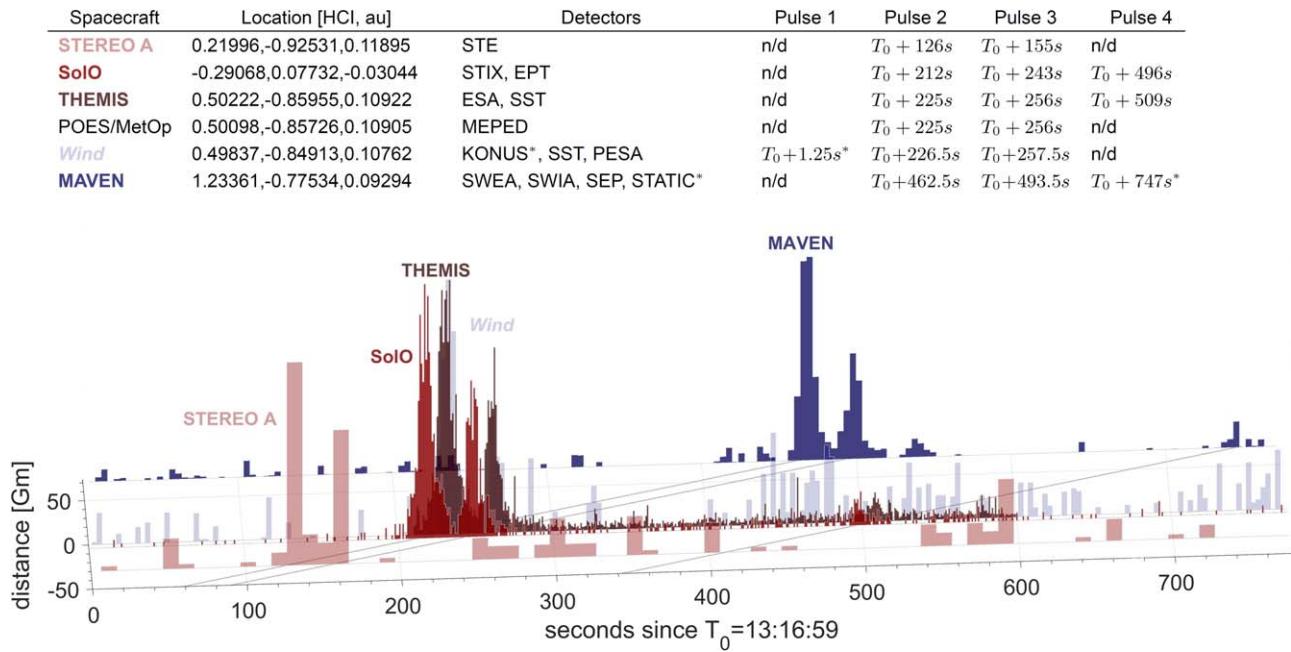


**Figure 5.** Propagation of the GRB221009A across the heliosphere. The temporal profiles of the gamma-ray burst signal detected by the charged particle detectors on board STEREO-A, SoIo, THC, Wind, and MAVEN are shown with different colors.  $T_0 = 13:16:59$ —time of the detection of the triggering impulse of GRB221009A in the vicinity of the Earth.  $y$ -axis—the distance between the points of observations along the normal to the signal front, where 0 is the position of the Earth. The normal was estimated based on the coordinates and times provided in the legend. Light-gray lines illustrate the propagation of Pulses 2, 3, and 4 of the GRB221009A with the speed of light.

STEREO, SoIo, and MAVEN. Positions of the spacecraft in the HCI coordinate system are listed in the legend of Figure 5. Using the start of the Pulse 2 detected at  $T_0 + 126 \pm 5$  s at STEREO-A,  $+212 \pm 0.5$  s at SoIo,  $+225 \pm 0.5$  s at THEMIS, and  $+462.5 \pm 1$  s at MAVEN, we estimated normal vector  $\mathbf{n} = [-0.6033, -0.3775, 0.7025]$  and the  $v = 1.01c$ . The normal vector gives the GRB221009A source location at R.A.  $288^\circ 5$ , decl.  $18^\circ 5$  in J2000 a cone of uncertainty (95% confidence level)  $\delta\theta = 2^\circ$ . Start times of the Pulse 2 were determined by comparing the temporal profiles with the profiles captured on THC (Agapitov et al. 2023; shown as gray dashed lines in Figures 2–4). In the case of MAVEN, the start of Pulse 2 was found to be at  $T_0 + 262$  s (STATIC) and  $T_0 + 263$  s (SWEA and SEP). In order to estimate the accuracy of the obtained values, we used the approach described in Vogt et al. (2011), which is based on the reciprocal vector formalism and takes into account uncertainties both in the crossing times and in the spacecraft positions.<sup>10,11</sup>

<sup>10</sup> The biggest source of the uncertainties is the STEREO time resolution of  $\Delta T = 10$  s. To estimate the influence of the spacecraft array geometry accuracy, we analyzed a position tensor in terms of its eigenvectors and the tetrahedron geometric parameters: planarity  $P$ , elongation  $E$ , and the RMS interspacecraft distance  $L$ . For the configuration of STEREO, SoIo, THC, and MAVEN,  $\delta\theta = v\Delta T/(L(1-E)) \sim 2^\circ$  and  $\delta v/v \sim 2\%$ .

<sup>11</sup> In the case of more than four spacecraft available and/or the preknown propagation speed (the speed of light), the least-squares method could be applied to solve the system (Paschmann & Daly 1998). For the GRB221009A case, adding data from Wind spacecraft results in values R.A.  $= 288^\circ 4$ , decl.  $= 18^\circ 9$ . The method could be used in the planar configuration if data are available from only three spacecraft. In this case, two components of the front normal can be found from the system of equations on the plane. An absolute value of the third component of the normal could be found if the speed of the front is known. Using data from THC, STEREO, and MAVEN in the  $(x-y)$  plane, one can find  $\mathbf{n} = [-0.5998, -0.4424, \pm 0.5047]$ . If a positive  $z$  component is taken, the location of the burst is R.A.  $= 292^\circ$ , decl.  $= 8^\circ$ . This method is less accurate than the one described above.

The obtained results are consistent with the previously reported values of R.A.  $= 288^\circ 282$ , decl.  $= 19^\circ 495 \pm 0^\circ 027$  (Pillera et al. 2022), R.A.  $= 288^\circ 2643$ , decl.  $= 19^\circ 7712$  (Dichiara et al. 2022) and R.A.  $= 287^\circ 761$ , decl.  $= 20^\circ 670$  (center; Kozyrev et al. 2022).

Figure 5 summarizes the observations of GRB221009A by the spacecraft across the heliosphere sorted along the normal to the GRB221009A signal front (the  $y$ -axis) on 2022 October 9. It shows the temporal profiles of the GRB signal recorded on STEREO-A, SoIo, THEMIS, Wind, and MAVEN, starting at  $T_0 = 13:16:59.000$ —time of the detection of the triggering signal (Pulse 1) of the GRB near the Earth (Veres et al. 2022). All of the listed spacecraft have detected the effects of Pulses 2 and 3, seen as two intense bursts. SoIo, THEMIS, and MAVEN have also captured Pulse 4. The speed-of-light signal propagation is marked by the light-gray lines.

## 5. Conclusion

We report the effects of the powerful gamma-ray burst GRB221009A recorded by the charged particle detectors on board the spacecraft probes at different locations across the heliosphere: Sun and solar wind observatories—STEREO-A, Solar Orbiter, and Wind; the magnetosphere multiprobe mission THEMIS; space weather probes at LEO orbits—POES/MetOp; and the planetary Martian mission MAVEN. GRB221009A had a structure of four bursts: the first triggering impulse was detected by the gamma-ray observatories near the Earth at  $T_0 = 13:16:59$  UT, the most intense Pulses 2 and 3, and less intense Pulse 4 were detected in the charged particle detector records (Pulse 4 in more than 500 s after the triggering Pulse 1). The effects of the GRB were detected at times corresponding to the spacecraft locations: STEREO-A detected the signal of Pulse 2 almost 100 s before it was detected in the vicinity of the Earth, and it took another  $\sim 237$  s for the signal















to reach MAVEN. Assuming that the burst propagated as a planar front across the heliosphere, we have determined the direction toward the source region of the GRB221009A at R.A. 288°5, decl. 18°5 with a 95% containment radius of 2°, for the first time, from multipoint observations of spacecraft-based particle detectors.

### Acknowledgments

The work was supported by NSF grant No. 1914670, NASA's Living with a Star (LWS) program (contract 80NSSC20K0218), and NASA grants contracts 80NNSC19K0848, 80NSSC22K0433, 80NSSC22K0522, 80NSSC20K0697, and 80NSSC21K177. We acknowledge NASA contract NAS5-02099 for the use of data from the THEMIS Mission and J. P. McFadden for the use of THEMIS ESA data and MAVEN STATIC data; J. Luhman for the use of STEREO-A data; Samuel Krucker for the use of SoLo STIX data. STEREO-A data were processed at SSL under NASA grant 80NSSC22K1359.

### ORCID iDs

Andrii Voshchepynets  <https://orcid.org/0000-0001-8307-781X>  
 Oleksiy V. Agapitov  <https://orcid.org/0000-0001-6427-1596>  
 Lynn Wilson, III  <https://orcid.org/0000-0002-4313-1970>  
 Vassilis Angelopoulos  <https://orcid.org/0000-0001-7024-1561>  
 Samer T. Alnussirat  <https://orcid.org/0000-0001-6125-6411>  
 Michael Balikhin  <https://orcid.org/0000-0002-8110-5626>  
 Myroslava Hlebena  <https://orcid.org/0000-0003-1100-515X>  
 Ihor Korol  <https://orcid.org/0000-0001-7826-0249>  
 Davin Larson  <https://orcid.org/0000-0001-5030-6030>  
 David Mitchell  <https://orcid.org/0000-0001-9154-7236>  
 Christopher Owen  <https://orcid.org/0000-0002-5982-4667>  
 Ali Rahmati  <https://orcid.org/0000-0003-0519-6498>

### References

- Acuña, M. H., Ogilvie, K. W., Baker, D. N., et al. 1995, *SSRv*, 71, 5  
 Agapitov, O. V., Balikhin, M., Hull, A. J., et al. 2023, *ApJL*, 948, L21  
 Angelopoulos, V. 2014, in *The ARTEMIS Mission*, ed. C. Russell & V. Angelopoulos (New York: Springer), 3  
 Aptekar, R. L., Frederiks, D. D., Golenetskii, S. V., et al. 1995, *SSRv*, 71, 265  
 Baktash, A., Horns, D., & Meyer, M. 2022, *arXiv:2210.07172*  
 Battiston, R., Neubüser, C., Follega, F. M., et al. 2023, *ApJL*, 946, L29  
 Brdar, V., & Li, Y.-Y. 2023, *PhLB*, 839, 137763  
 de Ugarte Postigo, A., Izzo, L., Pugliese, G., et al. 2022, *GCN*, 32648, 1  
 Diciara, S., Gropp, J. D., Kennea, J. A., et al. 2022, *GCN*, 32632, 1  
 Fränz, M., & Harper, D. 2002, *P&SS*, 50, 217  
 Frederiks, D., Lysenko, A., Ridnaia, A., et al. 2022, *GCN*, 32668, 1  
 Frederiks, D., Svinkin, D., Lysenko, A. L., et al. 2023, *ApJL*, 949, L7  
 Freedman, W. L. 2021, *ApJ*, 919, 16  
 Gompertz, B. P., Ravasio, M. E., Nicholl, M., et al. 2023, *NatAs*, 7, 67  
 Gotz, D., Mereghetti, S., Savchenko, V., et al. 2022, *GCN*, 32660, 1  
 Halekas, J. S., Taylor, E. R., Dalton, G., et al. 2015, *SSRv*, 195, 125  
 Hayes, L. A., & Gallagher, P. T. 2022, *RNAAS*, 6, 222  
 Jakosky, B. M., Lin, R. P., Grebowsky, J. M., et al. 2015, *SSRv*, 195, 3  
 Kaiser, M. L., Kucera, T. A., Davila, J. M., et al. 2008, *SSRv*, 136, 5  
 Kann, D. A., Agayeva, S., Aivazyan, V., et al. 2023, *ApJL*, 948, L12  
 Kann, D. A., & Agui Fernandez, J. F. 2022, *GCN*, 32762, 1  
 Kozyrev, A. S., Golovin, D. V., Litvak, M. L., et al. 2022, *GCN*, 32805, 1  
 Krucker, S., Hurford, G. J., Grimm, O., et al. 2020, *A&A*, 642, A15  
 Lapshov, I., Molkov, S., Mereminsky, I., et al. 2022, *GCN*, 32663, 1  
 Larson, D. A., Lillis, R. J., Lee, C. O., et al. 2015, *SSRv*, 195, 153  
 Laskar, T., Alexander, K. D., Margutti, R., et al. 2023, *ApJL*, 946, L23  
 Lesage, S., Veres, P., Briggs, M. S., et al. 2023, *ApJL*, 952, L42  
 Lesage, S., Veres, P., Roberts, O. J., et al. 2022, *GCN*, 32642, 1  
 Lin, R. P., Anderson, K. A., Ashford, S., et al. 1995, *SSRv*, 71, 125  
 Liu, J. C., Zhang, Y. Q., Xiong, S. L., et al. 2022, *GCN*, 32751, 1  
 Luhmann, J. G., Curtis, D. W., Schroeder, P., et al. 2008, in *STEREO IMPACT Investigation Goals, Measurements, and Data Products Overview*, ed. C. T. Russell (New York: Springer), 117  
 Lysenko, A. L., Ulanov, M. V., Kuznetsov, A. A., et al. 2022, *ApJS*, 262, 32  
 McFadden, J. P., Carlson, C. W., Larson, D., et al. 2008, *SSRv*, 141, 277  
 McFadden, J. P., Kortmann, O., Curtis, D., et al. 2015, *SSRv*, 195, 199  
 Mei, A., Banerjee, B., Oganessian, G., et al. 2022, *Natur*, 612, 236  
 Mitchell, D. L., Mazelle, C., Sauvaud, J. A., et al. 2016, *SSRv*, 200, 495  
 Mitchell, L. J., Phlips, B. F., & Johnson, W. N. 2022, *GCN*, 32746, 1  
 Müller St., D., Cyr, O. C., Zouganelis, I., et al. 2020, *A&A*, 642, A1  
 O'Connor, B., Troja, E., Ryan, G., et al. 2023, *SciA*, 9, eadi1405  
 Owen, C. J., Bruno, R., Livi, S., et al. 2020, *A&A*, 642, A16  
 Pal, S., Hobara, Y., Shvets, A., et al. 2023, *Atmos*, 14, 217  
 Paschmann, G., & Daly, P. W. 1998, *Analysis Methods for Multi-Spacecraft Data* (Noordwijk: ESA)  
 Pettit, J. M., Randall, C. E., Peck, E. D., & Harvey, V. L. 2021, *JGRA*, 126, e29667  
 Piano, G., Verrecchia, F., Bulgarelli, A., et al. 2022, *GCN*, 32657, 1  
 Pillera, R., Bissaldi, E., Omodei, N., et al. 2022, *GCN*, 32658, 1  
 Pisacane, V. L. 2005, *Fundamentals of Space Systems* (Oxford: Oxford Univ. Press)  
 Rastinejad, J. C., Gompertz, B. P., Levan, A. J., et al. 2022, *Natur*, 612, 223  
 Ripa, J., Pal, A., Werner, N., et al. 2022, *GCN*, 32685, 1  
 Rodger, C. J., Clilverd, M. A., Green, J. C., & Lam, M. M. 2010, *JGRA*, 115, A04202  
 Rodi, J., & Ubertini, P. 2023, *A&A*, 677, L3  
 Rodríguez-Pacheco, J., Wimmer-Schweingruber, R. F., Mason, G. M., et al. 2020, *A&A*, 642, A7  
 Sahu, S., Medina-Carrillo, B., Sánchez-Colón, G., & Rajpoot, S. 2023, *ApJL*, 942, L30  
 Schwartz, S. J., Zane, S., Wilson, R. J., et al. 2005, *ApJL*, 627, L129  
 Selesnick, R. S., Tu, W., Yando, K., Millan, R. M., & Redmon, R. J. 2020, *JGRA*, 125, e28240  
 Sibeck, D. G., & Angelopoulos, V. 2008, *SSRv*, 141, 35  
 Terasawa, T., Tanaka, Y. T., Takei, Y., et al. 2005, *Natur*, 434, 1110  
 Troja, E., Fryer, C. L., O'Connor, B., et al. 2022, *Natur*, 612, 228  
 Ursi, A., Panebianco, G., Pittori, C., et al. 2022, *GCN*, 32650, 1  
 Veres, P., Burns, E., Bissaldi, E., et al. 2022, *GCN*, 32636, 1  
 Vitale, V., Neubüser, C., Battiston, R., et al. 2023, *ApJ*, 952, 159  
 Vogt, J., Haaland, S., & Paschmann, G. 2011, *AnGeo*, 29, 2239  
 Wilson III, L. B., Brosius, A. L., Gopalswamy, N., et al. 2021, *RvGeo*, 59, e2020RG000714  
 Xiao, H., Krucker, S., & Daniel, R. 2022, *GCN*, 32661, 1